Design and Validation of a Multioutput Wireless Power Transfer System Using MPC Controller

Zhenxing Ye, *Student Member, IEEE*, and Ka Wai Eric Cheng, *Fellow, IEEE*

***Abstract*—This article presents a novel approach that combines Kalman filtering and model predictive control (MPC) algorithms to achieve stable output in a multioutput wireless power transfer (WPT) system for automated guided vehicles (AGVs). Traditional WPT systems often struggle to maintain stable output under varying load conditions and environmental disturbances, impacting the efficiency and reliability of AGV operations. To address this issue, we introduce a Kalman filter for real-time state estimation, coupled with an MPC algorithm for system prediction and control, thereby enhancing the system's robustness and dynamic response performance. Simulation and experimental results validate the superior performance of the proposed method under various operating conditions, demonstrating significant anti-interference capability and stable output characteristics. The results indicate that this method can markedly improve the stability and reliability of the AGV WPT system, providing strong technical support for its practical application.**

***Index Terms*—Automated guided vehicle (AGV), Kalman filter, model predictive control, multioutput, robustness, wireless power transfer.**

I. Introduction

AUTONOMOUS guided vehicles (AGVs) have revolutionized the logistics industry by enabling efficient and cost-effective material handling. As the demand for AGVs grows, so does the need for reliable and efficient power supply systems to support their operation. Wireless power transfer (WPT) technology offers a promising solution to address this challenge [1], [2], [3]. Wireless charging for AGV can be broadly categorized into two main types: dynamic WPT (DWPT) to facilitate charging while the vehicle is in motion and static WPT for stationary charging when the vehicle is parked [4], [5], [6].

When the AGV is parked, due to the parking position of the AGV, there will inevitably be a shift in position. The position of the wireless power transmitter and receiver coils will shift laterally, resulting in a change in the coupling relationship, the mutual inductance coefficient between the coils and the equivalent load of the system will change, leading to an unhealthy working condition of the system for a long time and the output power cannot be stabilized within the rated range [7], [8]. Effective measures are therefore required to enable the system to respond quickly and robustly to these conditions.

In response to the above problems, extensive research has been carried out at home and abroad in terms of system parameter optimization [9], resonant topology improvement [10], and multiple receiver coil power supply rail synergy [11] to improve the stability of wireless charging power.

In [9], by improving the topology of the resonant circuit, the method can maintain the relative stability of the system output power within a certain range, however, it cannot solve the problem of power fluctuation in the case of coil misalignment. In [9], [10], and [11], the problem of output power fluctuation due to coil offset is effectively reduced by the synergy of multiple receiving coils and supply rails, however, the design requires However, the design requires additional control strategies for vehicle position detection and guideway switching, which increases the cost and complexity of the overall system, and there is a cross-coupling problem to be solved when multiple coils are received and interleaved. On the other hand, in terms of related control strategy research, the use of controllers to regulate the system output power is constantly being proposed, which does not impose too many constraints on the system design, requires less hardware cost and is more adaptable [12].

In the literature [13], the basic characteristics are analyses for LCL-T-based wireless energy transmission systems and the corresponding small-signal model is established; a PI digital controller is used to make the output current regulation time shorter when the vehicle enters the charging area. However, the method only considers one-sided resonance compensation, which has problems such as poor antidrift performance and easy drift of electrical parameters at the receiver side. Hu et al. [14] used an SS-type compensation structure with a primary-side inverter circuit and a bilateral dc–dc regulator circuit as control objects and maximizes transmission efficiency by controlling the switching frequencies of these three objects. However, this method suffers from problems such as multiple control objects and difficulty in implementing the control algorithm. Using the robustness advantage of the μ controller, Xia et al. [15] used a closed-loop control strategy to monitor the output voltage in real-time and control the buck circuit on the supply side, providing a targeted solution to the problem of transmission power fluctuations caused by coil lateral offset. However, the

Manuscript received 2 April 2024; revised 14 June 2024; accepted 17 July 2024. Date of current version 7 October 2024. This work was supported by Research Grant Council under Grant 15207721 and Grant 15225422. Recommended for publication by Associate Editor M. Saeedifard. *(Corresponding author: Ka Wai Eric Cheng.)*

Zhenxing Ye is with the Department of Electrical and Electronic Engineering, The Hong Kong Polytechnic University, Hong Kong.

Ka Wai Eric Cheng was with the Hong Kong Polytechnic University, Hong Kong. He is now with the University of California, Merced, CA 95343 USA (e-mail: ericcheng@ucmerced.edu).

Color versions of one or more figures in this article are available at https://doi.org/10.1109/TPEL.2024.3434516.

Digital Object Identifier 10.1109/TPEL.2024.3434516

method has a long response time and requires real-time bidirectional communication, which makes it difficult to meet the requirements of fast response. In [16], a generalized state-space model was developed, and its dynamic response characteristics were analyzed based on the LCL-S resonant topology DWPT system, and a PI controller was used to regulate the output voltage; however, this method is cumbersome and complex to model the whole system. In [17], the amplitude and phase of the primary coil current were measured to derive the mutual inductance coefficient and the secondary load resistance, and an model predictive control (MPC) model was used to achieve constant output power control at the energy supply side, but this method only uses transfer functions to describe the system input–output relationship, which involves many parameters and does not describe the system dynamic characteristics well, and the controller performance is easily affected by parameter drift.

In the literature [18], a MPC method is proposed to achieve fast regulation of the load voltage of the dynamic WPT. A multistep predictive MPC control strategy is designed by means of sensor-to-sample time delays, which ultimately achieves 2 kW wireless energy transfer and is experimentally validated. However, the method requires real-time acquisition of Buck circuit inductor currents and capacitor voltages, storage and calculation of target data over a number of past acquisition cycles, making the control algorithm computationally intensive and the hardware implementation cost and space occupation high.

Based on the aforementioned surveys, this article presents a novel approach that combines Kalman filtering and MPC algorithms to achieve stable output in a multioutput WPT system for automated guided vehicles (AGVs). This proposed system proposes a multioutput model to regulate the output power after AGV misalignment, and the characteristics of this proposed method are as follows.

1) *Proposed Load Current Control Strategy:* We introduce a load current control strategy that combines MPC with Kalman filtering to achieve precise control of the load current under unilateral conditions. Leveraging the robustness of MPC, this strategy ensures stable output in a multioutput WPT system, enhancing system reliability and performance.
2) *Innovative Application of Kalman Filtering in WPT Systems:* The WPT system employs a Kalman filtering algorithm, enabling the estimation of the inductor current and capacitor voltage in a Buck circuit using only the load current measurement. This approach reduces the need for multiple sensors, simplifying the system design and reducing costs.
3) *System Modeling and Analysis through Quadratic Eigenvalue Problem:* The system is rigorously modeled and analyzed using the quadratic eigenvalue problem framework. This methodology facilitates the attainment of a fast-response constant current output, significantly improving the dynamic performance of the WPT system.

The rest of this article is organized as follows. The WPT system circuit analysis in Section II, the MPC algorithmic modeling in Sections III, IV, and V are simulation and experimental verification, respectively. Finally, Sections VI concludes this article.

II. Circuit Analysis

In magnetically coupled resonant WPT systems, the optimization of coil impedance can be achieved through the application of a resonant compensation topology. This approach aims to enhance the energy efficiency of the system. The LCC-S type of compensation network achieves a constant voltage output on the secondary side under the conditions of constant input voltage on the primary side and unchanged coil mutual inductance. Moreover, due to its straightforward secondary-side structure, it has found extensive applications in the field of dynamic WPT for electric vehicles [17].

In Fig. 1, the transfer of electrical energy to the secondary side is facilitated through a transmitter coil utilizing an LCC-S type resonant topology, which is then converted to dc through rectification and filtering processes. As different types and states of loads have different power requirements, a voltage conversion via a dc–dc converter is required. Given that a Buck circuit has a higher power control range than a Boost circuit under the same hardware conditions [17], a Buck circuit is used in this article. there is one transmitter and two receivers, each loosely coupled to the transmitting coil through mutual inductors M_{ps1} and M_{ps2}, respectively. L_p is the self-inductances of the transmitting coil, L_{s1} and L_{s2} are the self-inductances of the receiver coils. C_p, C_{s1}, and C_{s2} are the resonant capacitors used to compensate L_p, L_{s1}, and L_{s2} correspondingly. The input voltage and input current are denoted as U_p and I_p, respectively, while the current received at each terminal is denoted as I_{s1} and I_{s2}. The output voltage of the inverter is U_1 and the output current is I_1. In the Buck circuit, the currents through the inductor are I_{B1} and I_{B2} and the voltages across the capacitor are U_{B1} and U_{B2}, respectively. The currents on the loads are I_{L1} and I_{L2} , respectively.

R_{L1eq} and R_{L2eq} are the input equivalent loads of the rectifier and can be derived from the following equations:

$$R_{L1eq} = \frac{8}{\pi^2} R_{L1},\ R_{L2eq} = \frac{8}{\pi^2} R_{L2} \tag{1}$$

where R_{L1eq} and R_{L2eq} denote the load resistances at each receiving Terminal.

The full resonance condition of the system is

$$\omega^2 = \frac{1}{L_1 C_1} = \frac{1}{L_s C_s} = \frac{1}{(L_p - L_1)\, C_p}. \tag{2}$$

The output voltage U_{Fi} and the load received power P_{out} of the LCC-S topology can be expressed as

$$U_{Fi} \approx \frac{\omega^2 L_1 U_{in} R_{Lieq} M_{psi}}{\omega^2 L_1^2 R_{Lieq}} = \frac{U_{in} M_{psi}}{L_1}\ (i = 1\ or\ 2) \tag{3}$$

$$\begin{aligned} P_{\text{out}} &= P_{\text{out1}} + P_{\text{out2}} = \frac{U_{F1}^2}{R_{L1eq}} + \frac{U_{F2}^2}{R_{L2eq}} \\ &\approx \frac{U_{ino}^2}{L_1^2 R_{L1eq}} + \frac{U_{ino}^2}{L_2^2 R_{L2eq}} \end{aligned} \tag{4}$$

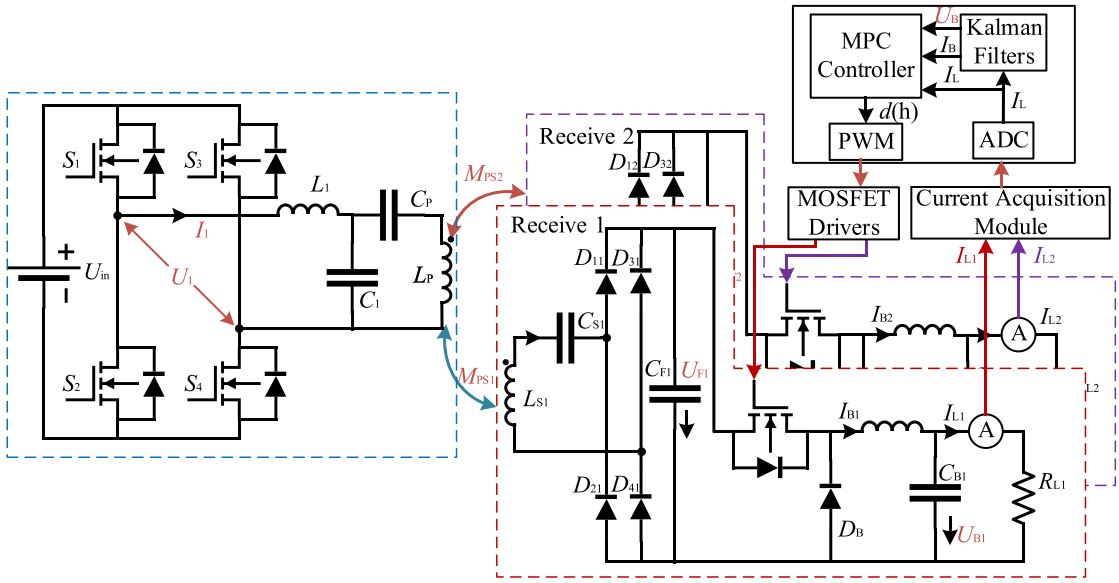

Fig. 1. Block diagram depicting the WPT system employing MPC control.

where ω is the operating angular frequency of the system and U_{ino} is the inverter output voltage

$$U_{ino} = 2\sqrt{2}\frac{U_{\text{in}}}{\pi}. \tag{5}$$

As can be seen from (3), the input voltage U_{F1} of the Buck circuit is positively related to the mutual inductance M_{ps1} or M_{ps2}. Fluctuations in the mutual inductance and the load will cause changes in the output voltage and power of the system. Therefore, to keep the charging current constant or to adjust the output power at the right time during vehicle driving and parking misalignment, it is necessary to control the load current I_{L1} or I_{L2} in a timely and effective manner to realize the control.

III. MPC Algorithmic Modeling

A. Modeling of Buck Circuits

To implement MPC in the entire control system, before proceeding, it is essential to develop a mathematical model of the object under control. According to the constant voltage output characteristics of the LCC-S resonant topology circuit demonstrated in session 2, the input voltage U_F of the Buck circuit can be treated as a constant voltage source at each sampling instant of the secondary side, making modeling more convenient. Since the system under discontinuous conduction mode (DCM) is more prone to problems such as sub-stability and instability, the mode is set in continuous conduction mode (CCM), where the switching transistor only operates in two states, namely ON and OFF, as illustrated in Fig. 2. Where I_B and U_B denote the current passing through the inductor and the voltage across the capacitor in the Buck circuit, respectively, while the switch transition time is ignored in the modeling process.

By modeling analysis using the equivalent circuit diagram described above, voltage across the capacitor and current through the inductor in the Buck circuit are selected as the system state variables, i.e., $\boldsymbol{X} = [U_B, I_B]^T$. The following equations,

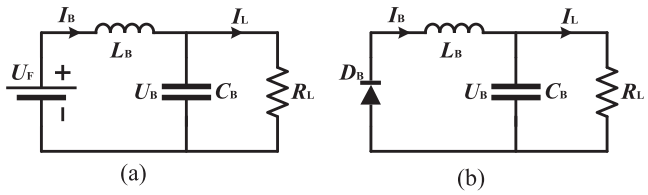

Fig. 2. This is a sample of a figure caption. (a) Switch ON state. (b) switch OFF state.

obtained using Kirchhoff's current and voltage laws, apply when the switch is ON and OFF, respectively.

Switch is ON

$$\begin{cases} C_B \frac{dU_B}{dt} = I_B - \frac{U_B}{R_L} \\ L_B \frac{dI_B}{dt} = U_F - U_B. \end{cases} \tag{6}$$

Switch is OFF

$$\begin{cases} C_B \frac{dU_B}{dt} = I_B - \frac{U_B}{R_L} \\ L_B \frac{dI_B}{dt} = -U_B. \end{cases} \tag{7}$$

Here, U_F denotes the input voltage of the Buck circuit, L_B denotes the inductance, C_B signifies the capacitance, I_B represents the voltage across the inductor, and U_B represents the voltage across the capacitor.

The equation of continuous state can be obtained as

Switch is ON

$$\boldsymbol{X'} = \begin{bmatrix} -\frac{1}{R_L C_B} & \frac{1}{C_B} \\ -\frac{1}{L_B} & 0 \end{bmatrix} \begin{bmatrix} U_B \\ I_B \end{bmatrix} + \begin{bmatrix} 0 \\ \frac{1}{L_B} \end{bmatrix} U_F = \boldsymbol{A}_1 \boldsymbol{X} + \boldsymbol{B}_1 U_F. \tag{8}$$

Switch is OFF

$$\boldsymbol{X'} = \begin{bmatrix} -\frac{1}{R_L C_B} & \frac{1}{C_B} \\ -\frac{1}{L_B} & 0 \end{bmatrix} \begin{bmatrix} U_B \\ I_B \end{bmatrix} = \boldsymbol{A}_1 \boldsymbol{X}. \tag{9}$$

Discretizing (8) and (9) gives

$$\boldsymbol{X}(h+1) = \boldsymbol{A}_2 \boldsymbol{X}(h) + \boldsymbol{B}_2 U_F. \tag{10}$$

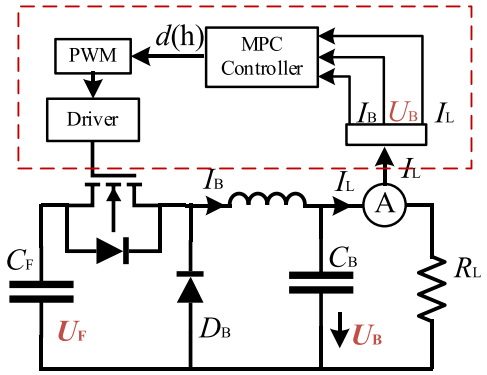

Fig. 3. Sketch of MPC controller.

Here, $\boldsymbol{A}_2 = \boldsymbol{I} + \boldsymbol{A}_1 dT + \boldsymbol{A}_1(1-d)T = \boldsymbol{I} + \boldsymbol{A}_1 T$, $\boldsymbol{B}_2 = \boldsymbol{B}_1 dT$, $\boldsymbol{I}$ is the unit matrix; d denotes the duty cycle of the switching tube, and its value range is 0∼1. T is the switching tube drive signal period.

Based on the properties of the topology of the LCC-S circuit in the previous section, the output can be considered as a constant voltage source U_F and taking the duty cycle d as the model input $u(h)$ and the load current I_L as the model output y, the discrete model of the Buck circuit is

$$\begin{cases} \boldsymbol{X}(h+1) = \boldsymbol{A_d}\boldsymbol{X}(h) + \boldsymbol{B_d}u(h) \\ y(h) = \boldsymbol{C_d}\boldsymbol{X}(h) \end{cases} \tag{11}$$

where $\boldsymbol{A_d} = (\boldsymbol{I} + \boldsymbol{A}_1 T)$, $\boldsymbol{B_d} = \boldsymbol{B}_1 T U_F$, $\boldsymbol{C_d} = \left[\frac{1}{R_L}, 0\right]$.

B. Model Predictive Controller Building

For analysis purposes, the circuit shown in Fig. 1 is simplified by adopting the configuration shown in Fig. 3.

Using the principles of the MPC algorithm, the augmentation matrix (12) and (13) have been formulated for the state space model (11) of the buck circuit

$$\begin{aligned} \begin{bmatrix} \boldsymbol{X}(h+1) \\ y(h+1) \end{bmatrix} &= \begin{bmatrix} \boldsymbol{A_d} & \boldsymbol{O}_n^T \\ \boldsymbol{C_d}\boldsymbol{A_d} & \boldsymbol{1} \end{bmatrix} \begin{bmatrix} \boldsymbol{X}(h) \\ y(h) \end{bmatrix} + \begin{bmatrix} \boldsymbol{B_d} \\ \boldsymbol{C_d}\boldsymbol{B_d} \end{bmatrix} u(h) \\ &= \boldsymbol{A_e} \begin{bmatrix} \boldsymbol{X}(h) \\ y(h) \end{bmatrix} + \boldsymbol{B_e} u(h) \end{aligned} \tag{12}$$

$$y(h) = [\boldsymbol{O}_n \ \boldsymbol{1}] \begin{bmatrix} \Delta\boldsymbol{X}(h) \\ y(h) \end{bmatrix} = \boldsymbol{C_e} \begin{bmatrix} \Delta\boldsymbol{X}(h) \\ y(h) \end{bmatrix}. \tag{13}$$

Here, $\boldsymbol{A_e} = \begin{bmatrix} \boldsymbol{A_d} & \boldsymbol{O}_n^T \\ \boldsymbol{C_d}\boldsymbol{A_d} & \boldsymbol{1} \end{bmatrix}$, $\boldsymbol{B_e} = \begin{bmatrix} \boldsymbol{B_d} \\ \boldsymbol{C_d}\boldsymbol{B_d} \end{bmatrix}$, $\boldsymbol{C_e} = [\boldsymbol{O}_n \ \boldsymbol{1}]$, $\boldsymbol{O}_n$ is the zero vector.

The purpose of building the augmentation matrix is to weaken the dynamic estimation error due to model parameter drift and to make the controller more focused on the state change trend and the target physical quantity, thus enhancing robustness to changes in mutual inductance coefficients and load values. Using the augmentation matrix, the state of the model over the next N_k sampling moments can be expressed in terms of the prediction equation as

$$\boldsymbol{Y_h} = \boldsymbol{F_h} \begin{bmatrix} X(h) \\ y(h) \end{bmatrix} + \boldsymbol{\Gamma_e} \boldsymbol{U_h} \tag{14}$$

where N_k is the prediction horizon and N_c is the control horizon

$$\boldsymbol{Y_h} = \begin{bmatrix} y(h|h) \\ y(h+1|h) \\ \cdots \\ x(h+N_k|h) \end{bmatrix}_{(nN_c)\times 1} \tag{15}$$

where $\boldsymbol{Y_h}$ is a $(nN_c) \times 1$ vector containing all the state variables in the prediction interval predicted at moment h. n is the dimension of the state matrix $\boldsymbol{A}_1$, here n is 2.

$$\boldsymbol{U_h} = \begin{bmatrix} u(h|h) \\ u(h+1|h) \\ \cdots \\ u(h+N_k-1|h) \end{bmatrix}_{(pN_k)\times 1} \tag{16}$$

where $\boldsymbol{U_h}$ is a $(pN_k) \times 1$ vector representing the sequence of control quantities (inputs) computed at the moment h. p is the dimension of the input matrix

$$\boldsymbol{F_h} = \begin{bmatrix} \boldsymbol{C_e}\boldsymbol{A_e} \\ \boldsymbol{C_e}\boldsymbol{A_e}^2 \\ \cdots \\ \boldsymbol{C_e}\boldsymbol{A_e}^{N_k} \end{bmatrix} \tag{17}$$

$$\boldsymbol{\Gamma_e} = \begin{bmatrix} \boldsymbol{C_e}\boldsymbol{B_e} & 0 & \cdots & 0 \\ \boldsymbol{C_e}\boldsymbol{A_e}\boldsymbol{B_e} & \boldsymbol{C_e}\boldsymbol{B_e} & \cdots & 0 \\ \boldsymbol{C_e}\boldsymbol{A_e}^2\boldsymbol{B_e} & \boldsymbol{C_e}\boldsymbol{A_e}\boldsymbol{B_e} & \cdots & 0 \\ \vdots & \vdots & \vdots & \vdots \\ \boldsymbol{C_e}\boldsymbol{A_e}^{N_k-1}\boldsymbol{B_e} & \boldsymbol{C_e}\boldsymbol{A_e}^{N_k-2}\boldsymbol{B_e} & \cdots & \boldsymbol{C_e}\boldsymbol{A_e}^{N_k-N_c}\boldsymbol{B_e} \end{bmatrix}. \tag{18}$$

The setting of the prediction horizons and control horizons can significantly impact the performance, stability, and robustness of an MPC system. Increasing the prediction horizon step size N_k generally increases the stability and robustness of the control system but reduces the dynamic response speed. In contrast, decreasing N_k can enhance the dynamic response speed, but at the cost of reduced stability and robustness. To achieve a faster response while maintaining stability, it is usually advisable to set a large N_k while keeping the control horizon length N_c less than or equal to N_k.

Build cost functions $\boldsymbol{J}$ based on tracking accuracy and control requirements

$$\boldsymbol{J} = (\boldsymbol{R_s} - \boldsymbol{Y_h})^T \hat{\boldsymbol{Q}} (\boldsymbol{R_s} - \boldsymbol{Y_h}) + \boldsymbol{U_h^T} \hat{\boldsymbol{R}} \boldsymbol{U_h} \tag{19}$$

where $\boldsymbol{R_s}$ is the reference matrix for the output.

According to (15), (16), (17), (18), and (19), the cost function can be simplified into a quadratic programming problem, resulting in the following ultimate form of the cost function:

$$\boldsymbol{J} = \boldsymbol{U_h^T}\boldsymbol{E} + \boldsymbol{U_h^T}\boldsymbol{H}\boldsymbol{U_h} \tag{20}$$

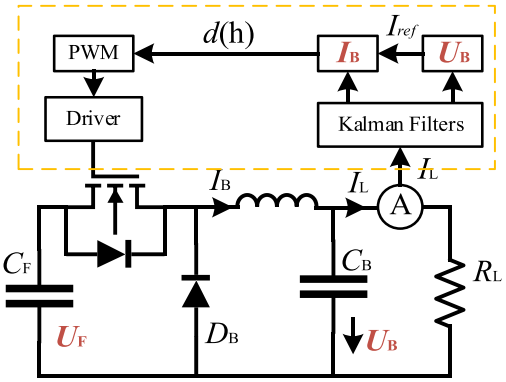

Fig. 4. Sketch of Kalman controller.

where $\boldsymbol{E} = 2\boldsymbol{\Gamma_e}\hat{\boldsymbol{Q}}\boldsymbol{F_h}[\boldsymbol{X}(h) - \boldsymbol{R_r}(h)]$, $\boldsymbol{H} = \boldsymbol{\Gamma_e^T}\ \hat{\boldsymbol{Q}}\boldsymbol{\Gamma_e} + \hat{\boldsymbol{R}}$, and $\boldsymbol{R_r}(h) = [0, \ldots, 0, ref(h)]^T$ is a matrix of the same dimension as $\boldsymbol{X}(h)$, and $ref(h)$ is the target reference value at time h. $\hat{\boldsymbol{Q}}$ and $\hat{\boldsymbol{R}}$ are the weight matrices, obtained by multiplying the weight constants q_w and r_w by the unit matrix $\boldsymbol{I}$, respectively. q_w and r_w together determine whether the solution process of the cost function is more concerned with the accuracy of control or the magnitude of the change in the control signal; increasing q_w increases the dynamic response speed and decreases the stability of the system, and vice versa; r_w has the opposite effect on the system as r_w, i.e., increasing r_w increases the stability of the system but slows down the dynamic response.

By solving the quadratic programming problem, the optimal duty cycle control signal, denoted as $\boldsymbol{U_h}$ at the current moment, is ultimately acquired [19]

$$\boldsymbol{U_h} = -\frac{2\boldsymbol{\Gamma_e}\hat{\boldsymbol{Q}}\boldsymbol{F_h}\left[\boldsymbol{X}\left(h\right) - \boldsymbol{R_r}\left(h\right)\right]}{\left[\boldsymbol{\Gamma_e^T}\ \hat{\boldsymbol{Q}}\boldsymbol{\Gamma_e} + \hat{\boldsymbol{R}}\right]}. \tag{21}$$

This process is carried out once per sampling cycle to enable rolling optimization to cope with the effects of various parameter drifts and external disturbances.

C. Kalman Filtered State Estimator

The model predictive controller introduced in the previous section requires three real-time measurements to be obtained at each control cycle, namely the capacitance-voltage U_B, the inductance current I_B, and the load current I_L, and using direct measurements would add additional hardware cost and space [20]. Equation (10) shows that the two state variables $[U_B, I_B]^T$ and the load current I_L can be correlated by this discrete model, so that the two state variables can be optimally estimated using a state estimation algorithm under the condition that only the load current I_L is measured.

For analysis purposes, the circuit shown in Fig. 1 is simplified by adopting the configuration shown in Fig. 4.

According to (11) and the principle of Kalman filtering algorithm, the state prediction $\boldsymbol{X}(h+1|h)$ and its covariance prediction $\boldsymbol{P}(h+1|h)$ at time h can be obtained as

$$\boldsymbol{X}\left(h+1|h\right) = \boldsymbol{A_d}\boldsymbol{X}\left(h|h\right) + \boldsymbol{B_d}d\left(h\right) \tag{22}$$

TABLE I
SIMULATION SETUP PARAMETER

Parameter	Values	Parameter	Values
Input voltage U_{in} (V)	40	Primary side inductor L_p(uH)	58.64
Operating frequency f (kHz)	85	Compensation capacitor C_s(nF)	72.66
Filter capacitors C_{Fl} (μF)	36.9	Secondary side inductors L_s(μH)	48.88
Mutual inductance M_{ps1} (μH)	9.785	Filter Inductors L_B(uH)	1300
Mutual inductance M_{ps2} (μH)	9.781	Filter Capacitor C_B(uF)	330
Coupling factor k_{ps1}	0.182	Noise covariance Q_w	10
Coupling factor k_{ps1}	0.182	Noise covariance R_v	5
Rated load R_{L1} and R_{L2}(Ω)	10	Predicted interval length N_p	5
Filter Capacitor C_1(nF)	452	Control interval length N_c	3
Compensation inductor L_1(μH)	7.8	Weighting constants q_w	1
Compensation capacitor C_p(nF)	69.1	Weighting constants r_w	0.01

$$\boldsymbol{P}\left(h+1|h\right) = \boldsymbol{A_d}\boldsymbol{P}\left(h|h\right)\boldsymbol{A_d^T} + Q_w \tag{23}$$

where Q_w is the system process noise covariance and $d(h)$ is the control signal from the controller.

Combining the system output measurements with the above state predictions, the optimal state estimate at time $h+1$ can be obtained as

$$\begin{aligned}&\boldsymbol{X}\left(h+1|h+1\right)\\ &= \boldsymbol{X}\left(h+1|h\right) + \boldsymbol{K}\left(h+1\right)\left[y\left(h+1\right) - \boldsymbol{C_d}\boldsymbol{X}(h+1|h)\right]\end{aligned} \tag{24}$$

where $\boldsymbol{K}(h+1)$ is the Kalman gain weight matrix

$$\boldsymbol{K}\left(h+1\right) = \frac{\boldsymbol{P}\left(h+1|h\right)\boldsymbol{C_d^T}}{\left[\boldsymbol{C_d}\boldsymbol{P}\left(h+1|h\right)\boldsymbol{C_d^T} + R_v\right]} \tag{25}$$

where R_v is the system measurement noise covariance.

This gives the state estimate at the current moment, and in order to be able to estimate the state again at the next moment, the covariance of the updated estimate $\boldsymbol{X}(h+1|h+1)$ is

$$\boldsymbol{P}\left(h+1|h+1\right) = \left[\boldsymbol{I} - \boldsymbol{K}\left(h+1\right)\boldsymbol{C_d}\right]\boldsymbol{P}\left(h+1|h\right). \tag{26}$$

The process is summarized as follows: the control signal $d(h)$ and the current measurement $y(h+1)$ at the current moment are fed into the Kalman filter and, after calculation by (22) to (26), the optimal estimate of the state variable at the current moment is obtained, which is then applied to the state estimation process at the next moment, and so on.

IV. SIMULATION VERIFICATION

To verify the efficacy of MPC in the output WPT system, we constructed a simulation model in the Simulink environment based on the circuit depicted in Fig. 1. When the circuit is in DCM, it affects the load transient response, increases the inductor ripple and output ripple, reduces the energy transfer efficiency, and the switching and conduction losses are usually higher. In order to obtain better overall performance and simpler control, the parameters of the circuit are designed, as shown in Table I, so that the system operates in CCM.

The prediction time domain step N_p and the control sequence dimension N_c directly affect the overall performance of the MPC

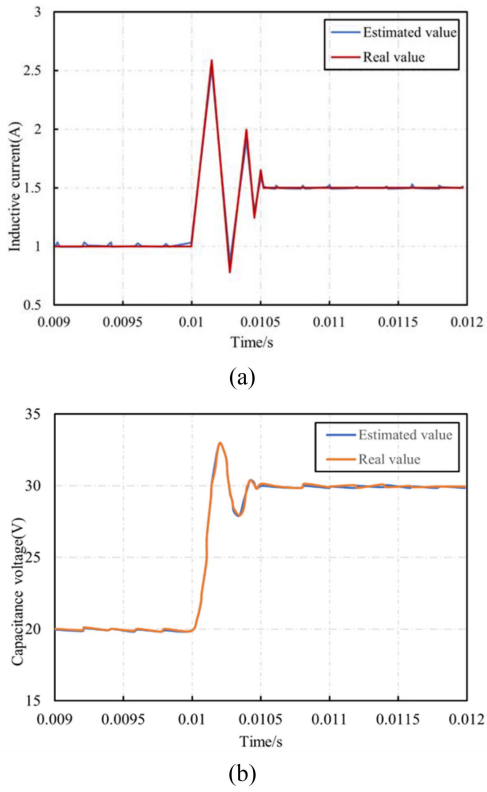

Fig. 5. Real and estimated. (a) Inductor currents. (b) Capacitance voltage.

controller, while the weight coefficients r_w and q_w influence the control accuracy of the MPC. Additionally, the system processes noise covariance Q_w and measurement noise covariance R_v determine the accuracy of the Kalman filter state estimation.

The parameter values given in Table I are the optimum results after several trials. The MPC is compared with one PI controller with different parameters, PI controller with P = 3.5e-5 and I = 2e-6. The PI control parameters are obtained by iteratively adjusting them according to the preset response waveform using the proportion integration differentiation (PID) tuner module of MATLAB/Simulink. The discrete sampling period of the simulation model and the output signal period of the controller are both 1e-5s. In the simulation, the output reference current, the mutual inductance value of the coil, and the load value are periodically varied. This variation is employed to replicate real-world scenarios, simulating conditions where the coil experiences offsets in practical applications.

A. Validation of Kalman Filter for Buck Circuits

The simulation of the system commences by validating the efficiency of the Kalman filter.

Fig. 5(a) and (b) shows the comparison between the estimated and actual values of the state variables $[U_B, I_B]^T$ of the Buck circuit obtained by the Kalman filter. The Kalman filter estimates of the variation of the capacitive voltage U_B and the inductive current I_B align well with the actual results, regardless of whether the system is in a steady state or step response process.

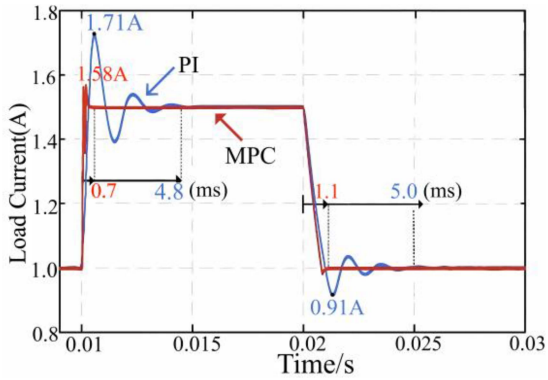

Fig. 6. Simulation results of MPC and PI controllers with suddenly changed reference current.

B. Comparison of WPT System Between MPC and PI Controller

First, set the initial reference value of the load current I_L to 1 A, and introduce a step change at 0.01 s and 0.02 s. Fig. 6 illustrates the responses of both the MPC controller and the PI controller to the step reference signal. From the graph, it can be observed that, after 0.01 s and 0.02 s, both controllers can accurately track the changes in the reference signal within a short time frame. However, it is noteworthy that, under the PI controller, the system exhibits more pronounced oscillations during tracking, indicating a significantly higher overshoot compared to the MPC controller. Furthermore, the stabilization time of the PI controller is also longer. In contrast, the MPC controller demonstrates a shorter stabilization time.

When the reference current changes from 1 A to 1.5 A, the overshoot of the MPC controller is only 0.08 A, and the reference tracking is completed within only 0.7 ms. When the reference current recovers to 1 A at 0.02 s, the MPC controller can reach a steady state within about 1.1 ms without obvious overshoot. In contrast, the PI controller has a slower response speed and a longer settling time of about 4.8 ms, when the reference current is from 1 A to 1.5 A, and up to 5.0 ms when the reference current is from 1.5 A to 1 A, and there is a potential risk of system device safety due to excessive overshoot. Therefore, compared to PI control, MPC control has a clear advantage in tracking speed and aligns better with the WPT system's requirements for rapid response.

In practical dynamic WPT charging systems, besides good wining techniques and coil design [18], coil misalignment is an inevitable phenomenon, which leads to fluctuations in the mutual inductance coefficient between coils. To ensure a prompt response, the controller must proficiently manage the dynamic disturbances in the mutual inductance coefficients within the WPT system.

Fig. 7 illustrates the responses of both the MPC controller and the PI controller to a jump in mutual inductance. When the mutual inductance changes from 8 μH to 5 μH at 0.01 s, the input voltage amplitude drops from 40 V to 27.8 V, and when the mutual inductance returns to 8 μH at 0.02 s, the input voltage also returns to 40 V. From Fig. 7, the mutual inductance changes

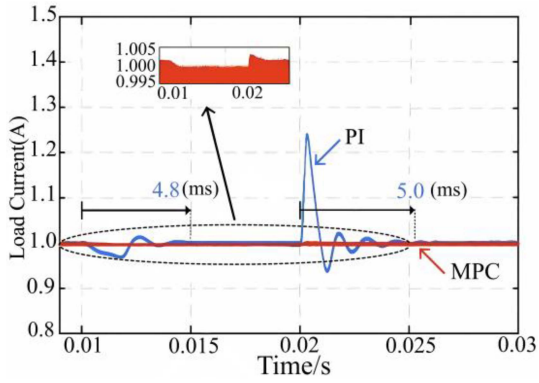

Fig. 7. Simulation results of MPC and PI controllers with suddenly changed mutual inductance.

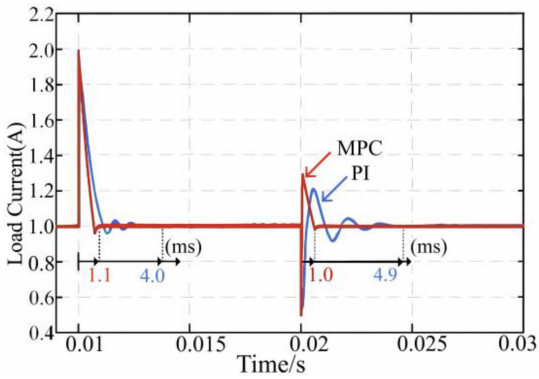

Fig. 8. Simulation results of MPC and PI controllers with suddenly changed load resistance.

at 0.01 s, and it takes 4.8 ms for the PI control to stabilize the load current; when the mutual inductance recovers from 5 μH the previous 8 μH at 0.02 s, the load current exhibits significant fluctuations under the influence of the PI controller, with occasional current peaks. However, upon closer inspection in the local magnified view, it can be observed that the load current exhibits minimal fluctuations under the MPC controller's influence, allowing for stable maintenance of the system's load current.

In addition, the stability of the system is significantly affected by dynamic changes in the load values. The following section presents the outcomes of testing various controllers for handling the dynamic load value perturbations.

Fig. 8 illustrates the responses of both the MPC controller and the PI controller during a load jump. The simulation sets the load resistance value to jump from 20 Ω to 10 Ω at 0.01 s, and then return to 20 Ω at 0.02 s. From the figure, it can be seen that at 0.01 s and 0.02 s load switching, the regulation time of the MPC controller is 1.1 ms and 1.0 ms, respectively, while the regulation times for the PI controller are 4.0 ms and 4.9 ms, respectively. As a result, MPC control has a significant advantage over PI control in terms of response time when the load resistance changes.

Considering all these findings collectively, it can be concluded that the MPC demonstrates resilience in the face of dynamic variations in mutual inductance and load. Consequently, the MPC approach is highly compatible with the robustness criteria of WPT systems.

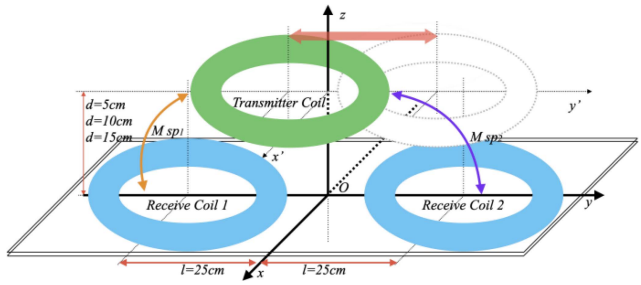

Fig. 9. Proposed structure with y-misalignments.

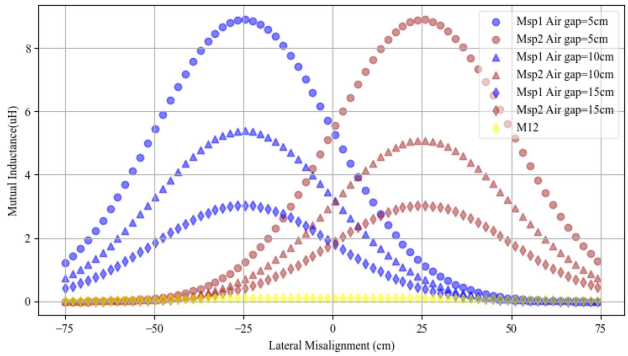

Fig. 10. Variation of the mutual inductance curve of a receiving coil misaligned with a transmitting coil.

C. Testing of Multioutput WPT Systems

In multioutput WPT systems, energy allocation and dynamic tuning are two key issues. Due to the limited energy of the transmitters and the possible interference between receivers, an effective energy allocation strategy is needed to ensure fairness and efficiency. At the same time, the system needs to have the prediction capability to dynamically adjust the energy allocation as the receiver energy demand changes so that the whole receiving system receives a stable amount of energy. The proposed structure with y-misalignment is shown in Fig. 9. The coil centers of receiver 1 and receiver 2 are located at −25 cm and 25 cm on the y-axis, respectively.

To enhance the fairness and efficiency of energy distribution, it is essential to consider the impact of nonalignment between coils. Fig. 10 shows the mutual inductance between the three coils for the misalignment case. As the receiver deviates along the y-axis within the range of [−75, 75] cm, M_{ps1} (M_{ps2}) increases as the receiver moves closer to the receiver 1 (receiver 2) coil, while M_{s1s2} is always very small, with a maximum value of 0.02 μH. Consequently, the cross-coupling between the receiver 1 and receiver 2 coils due to coil misalignment is negligible.

WPT of AGVs equipped with this system is susceptible to coil misalignment. For the purpose of this analysis, we assume that the misalignment occurs along the y-axis. Experimental testing of the current at receiver 1 (receiver 2) for various transmission distances, as depicted in Fig. 11, reveals the impact of the air gap on the stabilization of the received current. As shown, when

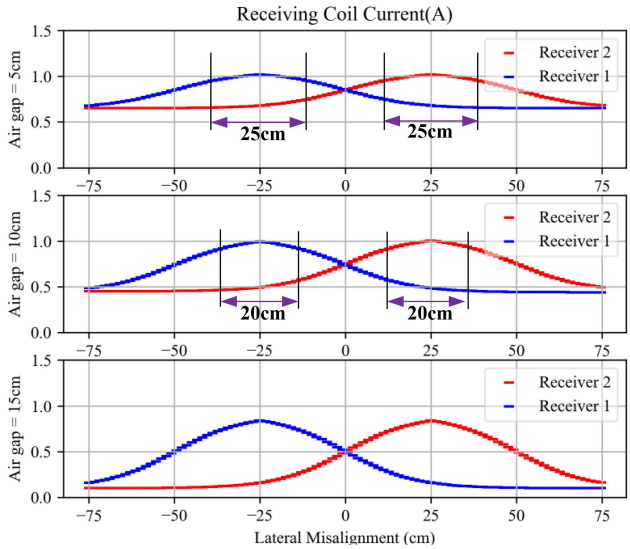

Fig. 11. Receiver coil current reference at various air gaps.

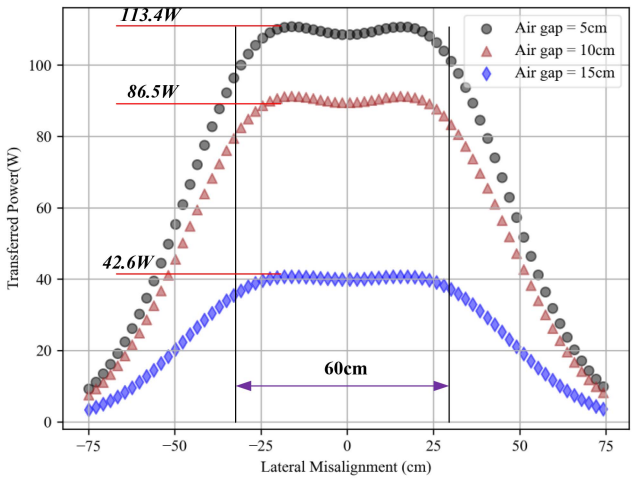

Fig. 12. WPT power profile for various air gaps.

the air gap is 5 cm, the current can be stabilized at 1 A within a distance of 25 cm from the center point's diameter; similarly, for an air gap of 10 cm, the current can be stabilized at 1 A within a distance of 20 cm. Notably, the effective transmission distance decreases with increasing air gap. When the air gap reaches 15 cm, the current does not reach 1 A. In summary, the proposed system, enabled by the MPC control system, enables the receiver to achieve a stabilized output over an effective transmission distance.

Fig. 12 shows the output power characteristics of our WPT system under different air gap distances and coil misalignment conditions. The results indicate that when the air gap is 5 cm, the system can achieve a maximum stable output power of 113.4 W within a lateral displacement range of ±30 cm. As the air gap distance increases, the maximum stable output power decreases. The variation in air gap distance affects the magnetic coupling strength and impedance matching between the transmit coil and the receive coil. An optimal air gap distance is crucial for maximizing energy transfer efficiency. However, excessive or

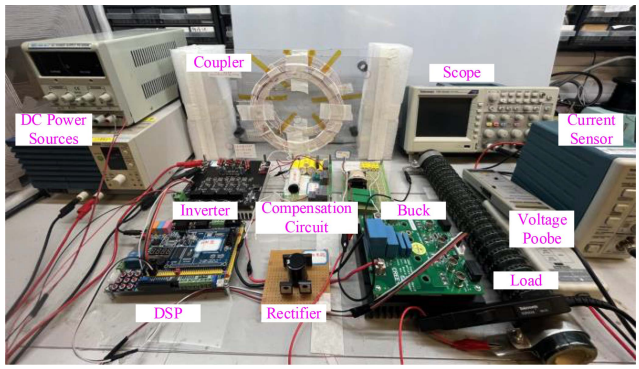

Fig. 13. Experimental bench for the proposed prototype.

TABLE II
COIL PARAMETERS

Coil	Internal Diameter(cm)	External Diameter(cm)	Number of turns
Transmitter coil	17	41	15
Receiver coil 1	17	40	12
Receiver coil 2	17	40	12

insufficient air gaps will reduce the coupling coefficient, limiting the power transmission capability.

Simulation results validate the high-efficiency output capabilities of our WPT system under coil misalignment conditions, while also emphasizing the importance of optimizing air gap distance for achieving high-efficiency energy transmission. To realize a more efficient dynamic wireless energy transfer system, further research is needed to investigate the effects of air gap distance, coil size, and structure on system output characteristics, providing guidance for achieving higher efficiency.

V. EXPERIMENTAL VERIFICATION AND ANALYSIS

To verify the effectiveness of the proposed method, we implemented a WPT system based on MPC control. Fig. 13 shows the test rig of the WPT system based on MPC control. The system consists of a dc power supply, a full-bridge inverter, coils, a resonance compensation network, a Buck circuit, and an electronic load. The proposed algorithm is implemented on a digital signal processor (DSP, TMS32028335). The Buck circuit uses the Model CRD8FF1217P-1 board, which uses high-performance SiC MOSFETs and SiC Schottky diodes to enable a fast-control Buck circuit. The switching frequency of the Buck circuit is 20 kHz, while the inverter operates at a switching frequency of 85 kHz.

A. Receiver Coil Position Design

The coil parameters of the system are shown in Table II, and the experimentally designed WPT system includes one transmitting coil and two receiving coils. Since the system is a multioutput system, in order to make the mutual inductance change of the transmitter coil and the receiver coil stable and smooth in the case of coil misalignment, and at the same time to ensure that the value of the mutual inductance is relatively large,

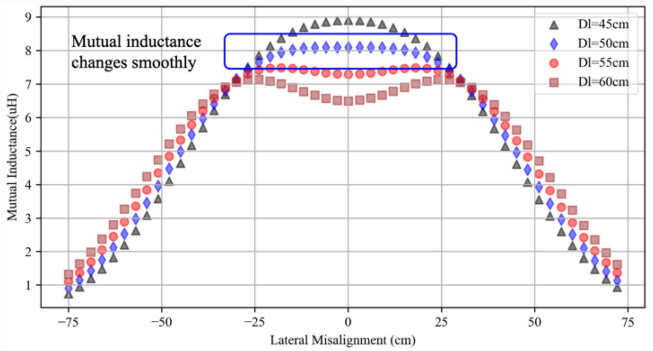

Fig. 14. Variation of mutual inductance at different distances from the receiving coil.

the experiment verifies the mutual inductance change of the two receiver coils at different distances (the distance D_l between the centres of the two receiver coils). The experimental results are shown in Fig. 14. When the two-receiver coil separation distance is less than 50 cm, the mutual inductance value is larger. However, when the coupling coils are misaligned, the mutual inductance variation is larger. On the other hand, when the two-receiver coil distance is larger than 50 cm, the mutual inductance value decreases, and the mutual inductance variation is larger. Hence comprehensive consideration of this article is to set the distance of two receiver coils for the best when the distance is 50 cm.

B. Comparison and Analysis of MPC and PI Controller

The fast response and stability of the system can be optimized by adjusting the parameters of the PI before the experiment. Fig. 15(a) and (b) compares the performance of the MPC controller and the PI controller in terms of reference value tracking. The waveforms displayed from top to bottom are the inverter output voltage, inverter output current, load current, and Buck circuit input voltage. Upon observing the graphs, it is evident that both MPC and PI controllers achieve accurate tracking of the reference value without overshooting, and their control errors are kept below 0.01 A. Although the two controllers perform similarly in terms of control accuracy, it is worth noting that the MPC controller has a significant advantage in terms of regulation time. When the reference value increased from 1 A to 1.5 A, the PI controller took 100 ms to complete the tracking. Upon restoring the reference value to 1 A, the PI controller required 101 ms to adjust. It is important to note that all evaluations presented here are objective and based solely on the data provided. In contrast, the MPC controller's average adjustment time for the same jumps was only about 14 ms, significantly less than that of the PI controller.

Thus, it can be inferred that the MPC controller demonstrates a faster response speed than the PI controller in the currently designed WPT system.

To verify the effect of different controllers when the mutual inductance mutates, experimental waveforms are shown in Fig. 16(a) and (b). The mutual inductance when the coils are fully aligned is approximately 9.78 μH. The experiment will move

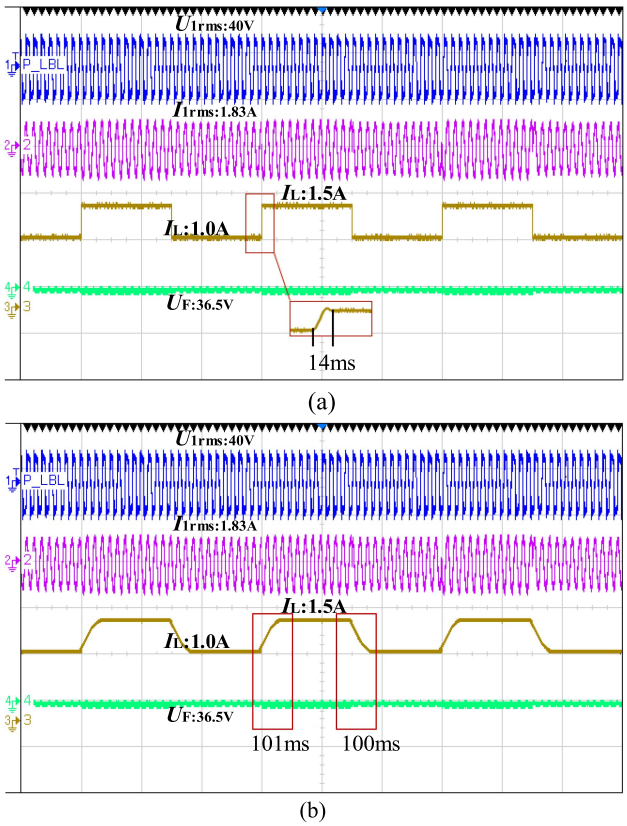

Fig. 15. Experimental results with suddenly changed reference current. (a) MPC controller. (b) PI controller.

the coil at the receiving end and misalign the mutual inductance coil to achieve the change in mutual inductance. The mutual inductance changes from 9.78 μH to 6.32 μH and then recovers to 9.78 μH.

Based on the experimental results, the input voltage of the Buck circuit reaches approximately 36.5 V when the induction coil is fully aligned. As the receiving end coil moves to a fixed position, the input voltage decreases to 24 V. Once the coil is restored to its initial position, the voltage quickly returns to 36 V. It is important to note that both the MPC and PI controllers perform equally well in terms of steady-state control accuracy. Additionally, they are both able to maintain stable control of the load current when the coil is moved. The PI controller has an average regulation time of approximately 116 ms. In contrast, the MPC controller maintains a stable load current throughout the process, demonstrating its robustness to mutual inductance changes. This finding is consistent with the simulation results presented in Fig. 7, which further confirms the superior performance of the MPC controller in handling mutual inductance variations.

Furthermore, the system's response was verified by abruptly changing the load resistance and connecting an electronic load. The load was varied from 20 Ω to 15 Ω and then restored to 25 Ω. The experimental results are shown in Fig. 17(a) and (b). It is evident that the MPC controller regulates the load current significantly faster than the PI controller when the load changes. The average adjustment time of the PI controller is

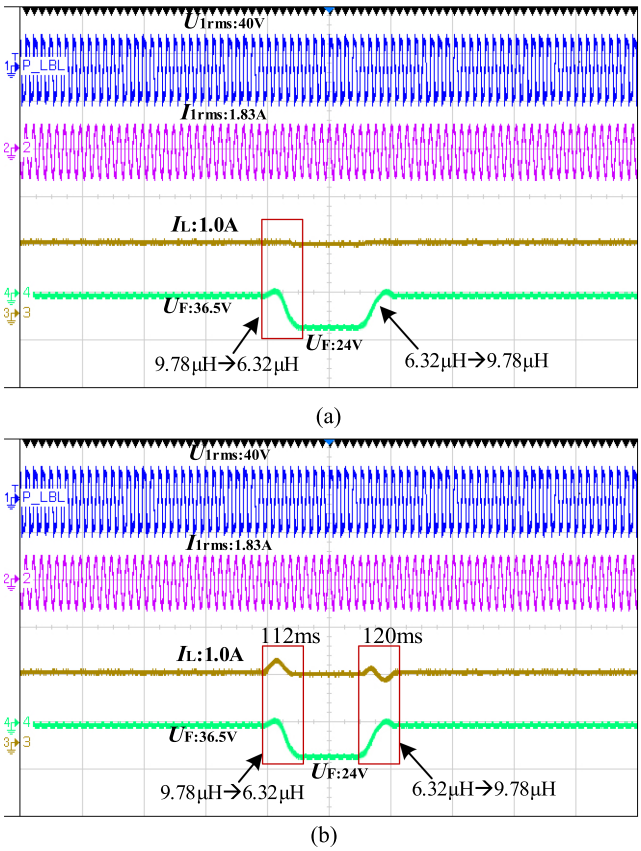

Fig. 16. Experimental results of MPC and PI controllers with suddenly changed mutual inductance. (a) MPC controller. (b) PI controller.

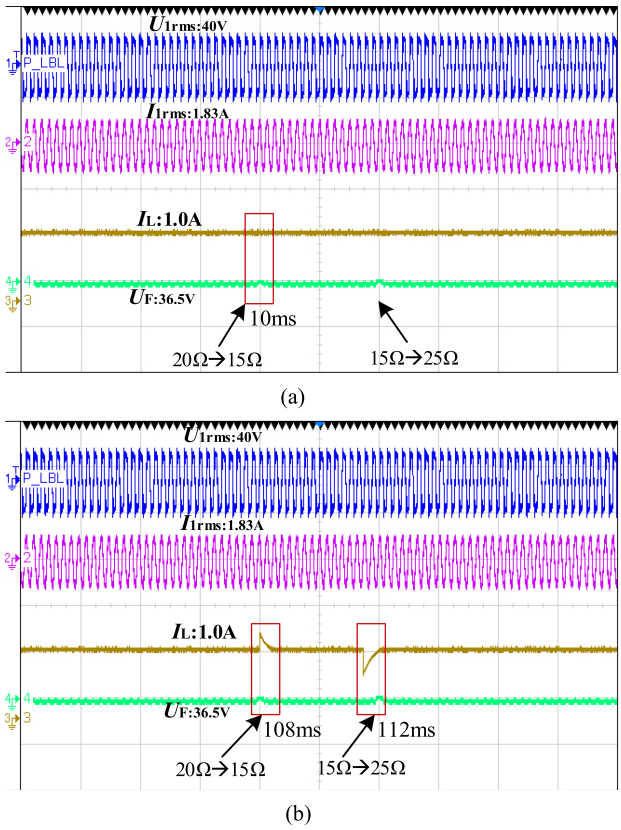

Fig. 17. Experimental results of MPC and PI controllers with suddenly changed load resistance. (a) MPC controller. (b) PI controller.

approximately 110 ms, whereas that of the MPC controller is only 10 ms. In comparison to the PI controller, the adjustment time is significantly reduced for the MPC controller.

C. Verification of Coil Misalignment WPT

Figs. 18–20 show the coil misalignment processes at the receiver side of a multioutput WPT system under different control strategies. It is then examining the transmitting coil to be aligned with the receiving coil 1 and the receiving coil 2, respectively, for a period of time from 0 to 1 s.

When the transmitting coil is aligned with the receiving coil 1 or coil 2, The waveforms under PI control exhibit increasing fluctuations, indicating system instability. This occurs because the system must adjust to the reference value for each coupling coefficient, which changes rapidly. The PI algorithm's regulation speed is insufficiently fast, leading to high-speed fluctuations. In an open-loop state, the output current converges slowly. In the system with the MPC algorithm, the output current rapidly stabilizes to the reference value as the transmitter coil is displaced from between the receiver coil 1 and the receiver coil 2. Furthermore, the MPC exhibits a high degree of tracking performance.

The experimental results demonstrate that the system with the MPC algorithm exhibits a short smoothing time and fast dynamic response, indicating that the MPC algorithm is well-suited to the WPT system.

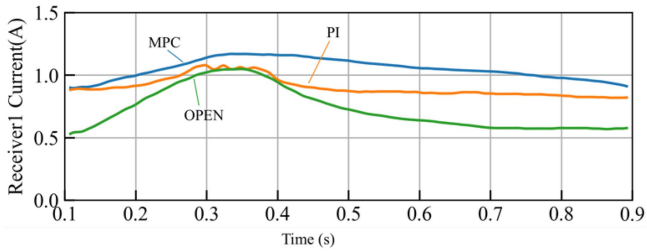

Fig. 18. Output current at receiver 1.

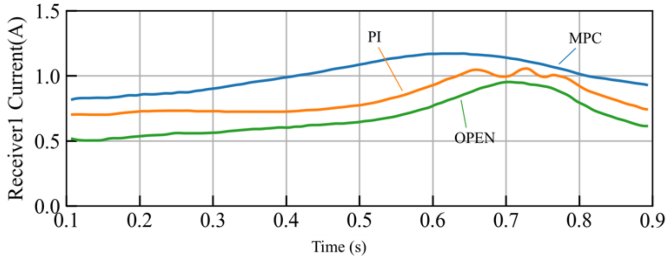

Fig. 19. Output current at receiver 2.

D. System Transmission Efficiency and Analysis

To determine the impact of various controllers on system transfer efficiency, this study tested output power using output power from 40 W to 120 W. The system transfer efficiency was then measured with no controller, MPC controller, and PI

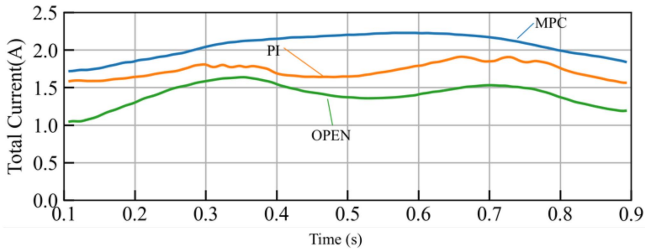

Fig. 20. Total current of the system output.

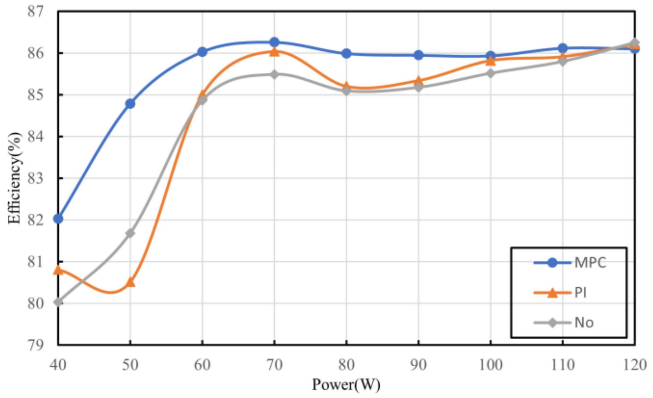

Fig. 21. Power transfer efficiency of the system.

controller. The results are presented in Fig. 21. As can be seen from the Fig. 21.

1) When the output power is less than 90 W, under the action of no controller, MPC controller and PI controller, when the output power is the same, the different control has a greater impact on the system. Under the MPC controller, the system has better transmission efficiency and the efficiency can reach up to 86.2%.
2) When the output power is greater than 90 W, in the absence of controller, MPC controller and PI controller, when the output power is the same, the system transmission efficiency is basically the same, indicating that the introduction of the controller does not bring a significant impact on the system transmission efficiency, but the MPC controller under the system transmission efficiency has been about 86%.

Analysis of the causes as follows.

1) This system's LCC-S topology is implemented on a primary side winding, exhibiting a constant current characteristic and thereby generating a stable loss allocation. As the output power increases, this allocation remains unchanged. However, when the system's output power continues to rise, its efficiency exhibits a slight decline. This is attributed to the fact that the current drawn by the system increases with increasing output power, leading to an increase in coil losses and other losses.
2) Under the control of the MPC system, the fast response of the system makes the output voltage of the buck circuit increase, and the efficiency also increases.

When the output power of the system continues to increase, the system efficiency decreases slightly. This is because the current of the system increases with the increase of the output power, which results in an increase in coil loss and other losses. The efficiency of the whole system is

$$\eta = \frac{P_{\text{out}}}{P_{\text{out}} + P_{\text{coil}} + P_{con} + P_{sw} + P_{inv}} \times 100\%. \tag{27}$$

The effective output power of the system is P_{out}, the coil power loss at the two receivers is P_{coil}, the conduction power loss of the MOSFETS is P_{con}, the switching power loss of the MOSFETS is P_{sw}, and the power loss of the passive rectifier is P_{inv} when the H-bridge inverter is in operation.

The measured power loss distribution is shown in Fig. 22 in three sections, rectifier, inverter and coupler section. According to the experimental power loss distribution, the power loss proportion of the coupler increases obviously, which is mainly generated by the coil loss. Specifically, when the output of the system is 120 W, the measured power loss distribution is shown in Fig. 22(b), where the measured results are obtained by making the difference between the measured input and output power of each unit of the system.

E. Comparative Analysis of the Proposed Method With Existing Control Strategies.

To further illustrate the advantages of the Kalman filter-MPC fusion method proposed in this article, we conduct a comprehensive comparison with existing approaches in the literature from multiple perspectives: resonant compensation topology, power control circuitry, bidirectional communication requirements on both primary and secondary sides, model dependency, test conditions for evaluating control effectiveness, and the number of parameters required for measurement. The results are summarized in Table III, which provides a detailed assessment of the complexity of the system modeling method employed and the level of model accuracy demanded by the control strategy. Zhou et al. [17] derived the load resistance and mutual inductance coefficients based on the system model to estimate the system output power, which requires high accuracy of the model. Chan et al. [20] used the finite control set (FCS)-MPC technique to control the output dc voltage and implements both maximum efficiency point tracking (MEPT) and bilateral soft switching, but the modeling process is complex.

This article adopts the LCC-S topology, the primary side has the coil constant current characteristics, the secondary side has the constant output voltage characteristics and the structure is simple, which is more suitable for the application of AGV charging. Adopting the secondary side Buck circuit to regulate the output power without communication between the primary and secondary sides of the system and reducing the number of required sensors by introducing the Kalman filter to estimate the inductor current and capacitor voltage of the Buck circuit online, which is helpful to saving the hardware cost and enhancing the system reliability. By adopting the incremental MPC control algorithm, the controller can better track the trend of the system state, thereby the incremental MPC control algorithm

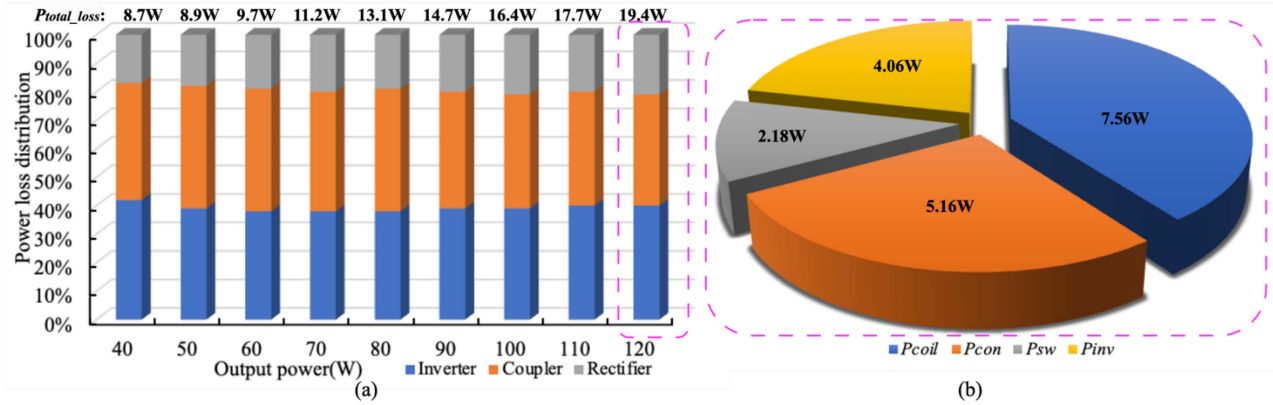

Fig. 22. Power loss distribution. (a) Power loss distribution versus the output power. (b) Power losses at the output power of 120 W.

TABLE III
COMPARISON OF THE PROPOSED METHOD WITH OTHER METHODS

Literatures	Control strategies	Topological circuit	Control circuits	Bilateral communication	Test conditions	Number of participants required
[16]	PI	LCC-S	Primary side inverter	Yes	Load	2
[17]	MPC	S-P	Primary side inverter	No	Mutual inductance	2
[18]	MPC	LCC-LCC	Secondary-side Buck	No	Mutual inductance, Reference value, Load	3
[21]	FCS-MPC	S-S	Primary side inverter, secondary side rectifier	Yes	Load	2
This article	Incremental MPC	LCC-S	Secondary-side Buck	No	Mutual inductance, Reference value, Load	1

allows the controller to focus on the trend of the system state, thus enhancing the robustness to changes in mutual inductance and load.

VI. CONCLUSION

To meet the requirements of fast response and high robustness of wireless power systems for AGVs under coil misalignment, this article proposes a load current control strategy based on the LCC-S compensation topology, combining Kalman filtering and MPC. A state-space model of the secondary side buck circuit is established, and a predictive controller is designed based on this model. By incorporating the Kalman filtering algorithm, stable control of the load current under single-parameter measurement conditions is achieved. A simulation model system is constructed to compare the proposed MPC controller with the traditional PI controller. The results indicate that, under similar transient conditions, the MPC controller exhibits significantly faster response speed than the PI controller and has strong robustness to mutual inductance and load variations. Meanwhile, the system efficiency under the MPC controller can reach 86%. Compared to other existing techniques, the proposed method does not require communication between the primary and secondary sides and has a lower dependence on the system model.

REFERENCES

[1] X. Mao, J. Lin, T. Su, and Y. Zhang, "Automatic guided vehicle wireless charging with dual receiving coils for misalignment tolerance," *IEEE Trans. Circuits Syst. II, Exp. Briefs*, vol. 71, no. 1, pp. 336–339, Jan. 2024, doi: 10.1109/TCSII.2023.3304661.

[2] Y. Li, J. Chen, Y. Liu, X. Zhao, M. Fu, and Z. He, "An accurate modeling and suppression method for current imbalance in dual-receiver WPT systems for low-voltage and High-current applications," *IEEE Trans. Transp. Electrific.*, to be published, doi: 10.1109 /TTE.2023.3345012.

[3] S. Pan, Y. Xu, Y. Lu, W. Liu, Y. Li, and R. Mai, "Design of compact magnetic coupler with low leakage EMF for AGV wireless power transfer system," *IEEE Trans. Ind. Appl.*, vol. 58, no. 1, pp. 1044–1052, Jan./Feb. 2022, doi: 10.1109/TIA.2021.3119906.

[4] L. Paolo, V. Cirimele, and A. Canova, "Economic and environmental sustainability of Dynamic Wireless Power Transfer for electric vehicles supporting reduction of local air pollutant emissions," *Renewable Sustain. Energy Rev.*, vol. 138, Mar. 2021, Art. no. 110537, doi: 10.1016/j.rser.2020.110537.

[5] L. Shuguang, Y. Zhenxing, and C. Gang, "Design and realization of high power density EV charging module," in *Proc. Chin. Control Decis. Conf.*, Nanchang, China, 2019, pp. 4909–4913, doi: 10.1109/CCDC.2019.8832920.

[6] K. Wang, Y. Yang, H. Wang, and E. K. W. Cheng, "Frequency regulation scheme for double-Sided LCC compensated inductive power transfer systems with Quasi-load-independent outputs," in *Proc. IEEE Energy Convers. Congr. Expo.*, Nashville, TN, USA, 2023, pp. 6383–6388, doi: 10.1109/ECCE53617.2023.10362732.

[7] Y. Li, J. Hu, X. Li, H. Wang, and K. W. E. Cheng, "Cost-Effective and compact multistring LED driver based on a three-coil wireless power transfer system," *IEEE Trans. Power Electron.*, vol. 34, no. 8, pp. 7156–7160, Aug. 2019, doi: 10.1109/TPEL.2019.2899454.

[8] H. Wang and K. W. E. Cheng, "A dual-receiver inductive charging system for automated guided vehicles," *IEEE Trans. Magn.*, vol. 58, no. 8, Aug. 2022, Art. no. 8700905, doi: 10.1109/TMAG.2022.3181576.

[9] K. Chen, K. W. E. Cheng, Y. Yang, and J. Pan, "A fast self-positioning-based optimal frequency control for inductive wireless power transfer systems without communication," *IEEE Trans. Ind. Electron.*, vol. 70, no. 1, pp. 334–343, Jan. 2023, doi: 10.1109/TIE.2022.3148758.

[10] S. Li, L. Wang, Y. Guo, C. Tao, and L. Ji, "Power stabilization with double transmitting coils and T-type compensation network for dynamic wireless charging of EV," *IEEE J. Emerg. Sel. Topics Power Electron.*, vol. 8, no. 2, pp. 1801–1812, Jun. 2020, doi: 10.1109/JESTPE.2019.2915551.

[11] H. Wang and K. W. E. Cheng, "An improved and integrated design of segmented dynamic wireless power transfer for electric vehicles," *Energies*, vol. 14, no. 7, Apr. 2021, Art. no. 1975, doi: 10.3390/en14071975.
[12] T. Hua, M. Chen, and K. W. E. Cheng, "Magnetic power distribution using controlled permeability bypass and its multiple output investigation," *IEEE Trans. Power Electron.*, vol. 38, no. 11, pp. 14734–14746, Nov. 2023, doi: 10.1109/TPEL.2023.3302619.
[13] H. Hao, G. A. Covic, and J. T. Boys, "An approximate dynamic model of LCL-T-based inductive power transfer power supplies," *IEEE Trans. Power Electron.*, vol. 29, no. 10, pp. 5554–5567, Oct. 2014, doi: 10.1109/TPEL.2013.2293138.
[14] X. Hu, Y. Wang, Y. Jiang, W. Lei, and X. Dong, "Maximum efficiency tracking for dynamic wireless power transfer system using LCC compensation topology," in *Proc. IEEE Energy Convers. Congr. Expo.*, Portland, OR, USA, 2018, pp. 1992–1996, doi: 10.1109/ECCE.2018.8557494.
[15] C. Xia, W. Wang, S. Ren, X. Wu, and Y. Sun, "Robust control for inductively coupled power transfer systems with coil misalignment," *IEEE Trans. Power Electron.*, vol. 33, no. 9, pp. 8110–8122, Sep. 2018, doi: 10.1109/TPEL.2017.2771532.
[16] S. Sasikumar and K. Deepa, "Comparative study of LCL-S and LCC-S topology of wireless EV charging system," in *Proc. Innovations Power Adv. Comput. Technol.*, Vellore, India, 2019, pp. 1–6, doi: 10.1109/i-PACT44901.2019.8960121.
[17] Z. Zhou, L. Zhang, Z. Liu, Q. Chen, R. Long, and H. Su, "Model predictive control for the receiving-side DC–DC converter of dynamic wireless power transfer," *IEEE Trans. Power Electron.*, vol. 35, no. 9, pp. 8985–8997, Sep. 2020, doi: 10.1109/TPEL.2020.2969996.
[18] A. G. Beccuti, S. Mariethoz, S. Cliquennois, S. Wang, and M. Morari, "Explicit model predictive control of DC–DC switched-mode power supplies with extended kalman filtering," *IEEE Trans. Ind. Electron.*, vol. 56, no. 6, pp. 1864–1874, Jun. 2009, doi: 10.1109/TIE.2009.2015748.
[19] J. B. Rawlings, "Tutorial: model predictive control technology," in *Proc. Amer. Control Conf. (Cat. No. 99CH36251)*, San Diego, CA, USA, 1999, vol. 1, pp. 662–676, doi: 10.1109/ACC.1999.782911.
[20] H. L. Chan, K. W. E. Cheng, and D. Sutanto, "A simplified Neumann's formula for calculation of inductance of spiral coil," in *Proc. Int. Conf. Power Electron. Variable Speed Drives*, 2000, Art. no. 475.
[21] C. Qi, Z. Lang, L. Su, X. Chen, and H. Miao, "Finite-Control-Set model predictive control for a wireless power transfer system," in *Proc. IEEE Int. Symp. Predictive Control Elect. Drives Power Electron.*, Quanzhou, China, 2019, pp. 1–5, doi: 10.1109/PRECEDE.2019.8753247.

Zhenxing Ye (Student Member, IEEE) received the B.Sc. degree in electrical engineering from Huangshan University, Huangshan, China, in 2018, and the M.Sc. degree in control engineering from Xi'an Polytechnic University, Xi'an, China, in 2022. He is currently working toward the Ph.D. degree in power electronics with the Department of Electrical and Electronic Engineering, Faculty of Engineering, Hong Kong Polytechnic University, Hong Kong.

In 2021, he was with Laboratory for Artificial Intelligence in Design, as a Research Assistant. His current research interests include inductive/wireless power transfer, electric vehicles, object detection, autonomous Driving, and artificial intelligence.

Ka Wai Eric Cheng (Fellow, IEEE) received the B.Sc. degree in electrical and electronic engineering and the Ph.D. degree in power electronics from the University of Bath, Bath, U.K., in 1987 and 1990, respectively.

Before joining The Hong Kong Polytechnic University, Hong Kong, in 1997, he was with Lucas Aerospace, London, U.K., as a Principal Engineer. He is currently a Professor with the Department of Electrical and Electronic Engineering, Faculty of Engineering, University of California, Merced. He has authored or coauthored more than 400 articles and seven books. His research interests include all aspects of power electronics, motor drives, electromagnetic interference, electric vehicles, battery management, and energy saving.

Dr. Cheng was a recipient of the Institution of Electrical Engineers Sebastian Z De Ferranti Premium Award, in 1995, the Outstanding Consultancy Award, in 2000, the Faculty Merit Award for Best Teaching from The Hong Kong Polytechnic University, in 2003, the Faculty Engineering Industrial and Engineering Services Grant Achievement Award, in 2006, the Brussels Innova Energy Gold Medal with Mention, in 2007, the Consumer Product Design Award, in 2008, the Electric Vehicle Team Merit Award of the Faculty, in 2009, the Eco Star Award, in 2012, the Gold Prize at Seoul International Invention Fair, in 2015, the iCAN Gold Medal at Canada for contribution in active suspension, in 2016, the Gold Award of HK Innovation and Technology for contribution in body integrated supercapacitor for vehicles, in 2017, the Geneva Invention Expo Silver Medal for contribution in e-Antilock braking systems, in 2021, and TechConnect 2023 and Geneva Invention Expo Silver Medal 2024 for the Innovation in Ammonia Electric Vehicles.